ChemSusChem

Research Article
doi.org/10.1002/cssc.202401970

Chemistry Europe
European Chemical Societies Publishing

www.chemsuschem.org

Electrified Dynamically Responsive Ammonia Decomposition to Hydrogen Based on Magnetic Heating of a Ru Nanocatalyst

Žiga Ponikvar,*[a, b] Anja Sedminek,[a, b] Janvit Teržan,[c] Luka Skubic,[a, b] Žan Lavrič,[c, d] Matej Huš,[c, d, e, f] Miha Grilc,[c, d] Blaž Likozar,*[c] Darko Makovec,[a] and Sašo Gyergyek*[a]

Storing and transporting pressurized or liquid hydrogen is expensive and hazardous. As a result, safer methods, such as chemical storage in ammonia, are becoming increasingly important. However, the instantaneous start of a conventionally heated decomposition reactor is challenging. Here we report on the electrified and dynamically responsive decomposition of ammonia as a means of releasing on-demand chemically bonded hydrogen based on the rapid magnetic heating of a well-designed Ru-based nanocomposite catalyst. Under relatively mild conditions (400 °C, 1 bar) a rapid decomposition rate of 5.33 $mol_{NH3}\,g_{Ru}^{-1}\,h^{-1}$ was achieved. Experimental observations under non-isothermal, dynamic conditions coupled with modelling at the level of density functional theory and micro-kinetic modeling confirmed the minute-scale response of the H_2 release. The rapid response of our catalytic system would, at least in principle, enable the utilization of intermittent, renewable electricity and a tunable H_2/NH_3 ratio in the reactor's effluent.

Introduction

Renewable, carbon-free energy carriers such as hydrogen are attracting a lot of attention, primarily for use in fuel cells. It is an emerging technology that is currently bottlenecked by hydrogen-storage limitations. Due to hydrogen's extremely low critical temperature, high-pressure storage is prone to accidents, especially if such approaches are implemented for vehicular and other on-demand applications.[1] A viable solution would be to store the hydrogen in a stable molecule that is also capable of releasing the hydrogen (the energy vector) on demand. One such molecule is ammonia (NH_3). It has a high hydrogen-storage capacity and high energy density compared to other hydrogen-carrier candidates, e.g., porous materials, metal hydrides, and hydrocarbons.[2–10]

Ammonia contains 17.8 wt% hydrogen and can be liquefied at low pressures, i.e., just 8.6 bar at 20 °C.[1] Its ability to be readily stored in liquid form makes it convenient for transportation and on-the-spot hydrogen production when required. In addition to its hydrogen-storage capacity, ammonia has already proven to be suitable for use in internal combustion engines as a stand-alone fuel and in dual-fuel mode combined with conventional liquid fuels.[11,12] Experimental studies focusing on variable hydrogen–ammonia mixtures have already been conducted. These mixtures represent a carbon-free alternative to the current selection of fossil fuels.

Ammonia-hydrogen mixtures compensate for the low flame speed of ammonia and also the high flame speed of hydrogen (problems with knocking).[13] The octane rating of both ammonia and hydrogen is higher than gasoline, making it more suitable to run at a higher compression ratio.[14] Mørch *et. al.* made a series of experiments by feeding a spark ignition (SI) engine with a varying excess-air ratio and different ammonia-to-hydrogen ratios.[14] The study showed that a gaseous fuel mixture with 10 vol% hydrogen performs best with respect to efficiency and power.[14] A comparison with a gasoline-fed SI engine was also made.[14] It showed that the efficiencies and power increased due to the possibility of a higher compression ratio.[14] The study also showed that the ammonia-to-hydrogen ratio represents a new, possible engine-control parameter.[14] Even though the NO_x emissions are reportedly high, employing a well-known DeNOx technology mitigates the issue.[15–18] It is not difficult to imagine that the filling stations of the future will need to provide electricity charging stations for standard electric vehicles (EVs), H_2 for the fuel-cell-powered EVs and ammonia and ammonia/H_2 mixtures for SI-engine-powered

[a] *Department for Synthesis of Materials, Jožef Stefan Institute, Ljubljana, Slovenia*
[b] *Faculty of Chemistry and Chemical Technology, University of Maribor, Maribor, Slovenia*
[c] *Department of Catalysis and Chemical Reaction Engineering, National Institute of Chemistry, Ljubljana, Slovenia*
[d] *Graduate School, University of Nova Gorica, Nova Gorica, Slovenia*
[e] *Association for Technical Culture of Slovenia, Ljubljana, Slovenia*
[f] *Institute for the Protection of Cultural Heritage of Slovenia, Ljubljana, Slovenia*

Correspondence: *Žiga Ponikvar and Sašo Gyergyek, Department for Synthesis of Materials, Jožef Stefan Institute, Jamova cesta 39, 1000 Ljubljana, Slovenia.*
Email: ziga.ponikvar@ijs.si and saso.gyergyek@ijs.si

Blaž Likozar, Department of Catalysis and Chemical Reaction Engineering, National Institute of Chemistry, Hajdrihova 19, 1000 Ljubljana, Slovenia.
Email: blaz.likozar@ki.si

Supporting information for this article is available on the WWW under https://doi.org/10.1002/cssc.202401970

vehicles such as heavy-duty trucks and agricultural machinery. Therefore, a technological solution capable of providing on-demand, pure H_2 from ammonia at the filling station and on-board H_2/NH_3 mixtures with a variety of ratios is needed.

Ammonia can be catalytically decomposed according to the reaction below at elevated temperatures:

$$2NH_3 \rightleftharpoons N_2 + 3H_2 \ (\Delta G^0 = -33 \text{ kJ mol}^{-1},\ \Delta H^\circ = 92 \text{ kJ mol}^{-1})$$

The decomposition reaction is endothermic and reaches >99% conversion at around 400 °C and 1 bar according to the thermodynamic equilibrium, assuming the inlet flow is pure ammonia.[1] However, without the aid of an appropriate catalyst, the decomposition reaction does not proceed, even at temperatures as high as 700 °C.[19–21] Many studies, experimental and theoretical, for example, Jacobsen et al. (volcano plot)[22] show that among the single-metal catalysts, Ru has the highest activity.[19–21]

An ammonia-decomposition reactor can be heated by different sources, such as gas burners or electrical resistance-based heating elements positioned around or within the pressure vessel.[23] Magnetic heating of the catalyst, however, could mitigate the poor temperature response of these systems. A composite catalyst can be embedded with ferromagnetic nanoparticles and placed in an alternating magnetic field, yielding reaction heat in terms of seconds. Within the nanoparticles, heat is produced and transferred to the surrounding catalyst support decorated with catalytic nanoparticles (NPs) where the reaction proceeds. When a susceptor is placed in an AC magnetic field, contactless RF energy transfer occurs. The generation of the heat is accompanied by only minor energy losses due to convection, conduction or thermal radiation.[24] Depending on the nature of the susceptor material, three main electromagnetic phenomena are responsible for the heat generation. In the case of ferromagnetic materials, hysteresis heating is caused by cycling through the material's magnetic hysteresis loop. Superparamagnetic NPs are subject to relaxation losses (the Néel relaxation mechanism), while electrically conductive samples experience eddy currents. Consequently, Joule heating occurs due to the material's resistance (the two effects combined are commonly referred to as induction heating).[24] It should be noted that relaxation losses have been studied for many years for the treatment of cancer using the so-called magnetic hyperthermia approach.[25–27] The phenomenon, however, has only received modest attention in recent years for catalysis.[28–30] Among the different magnetic nanoparticles, magnetic iron oxide (magnetite, Fe_3O_4) nanoparticles are commonly used due to their simple synthesis, the low cost of the starting materials (ferrous and ferric sulphate, for example), while they have excellent heating capabilities.[31–33] Nevertheless, the atmosphere within the ammonia-decomposition reactor is highly reducing, which would lead to the formation of non-magnetic wüstite (FeO) and consequently a loss of magnetic properties.[7] Almind et al. prepared catalysts composed of Co_xNi_{1-x} (x from 0.2–0.6) alloy nanoparticles dispersed on alumina that showed stable magnetic properties under magnetically heated steam-methane reforming.[34,35] The alloy nanoparticles had a high Curie temperature, ranging from 617 °C to 921 °C as x increased from 0.2–0.6, suggesting they could be used as a susceptor for ammonia decomposition. Inspired by their work, we developed a nanocomposite catalyst composed of $Co_{0.67}Ni_{0.33}$ nanoparticles embedded within an alumina matrix decorated with Ru nanoparticles. The ferromagnetic nature of the CoNi magnetic nanoparticles was used to convert RF energy into heat as a result of the hysteresis losses. To differentiate between these mechanisms, the corresponding heating mechanism is referred to here as magnetic heating. In the present study, we describe a method of electrified ammonia decomposition by magnetic heating of a well-designed catalyst that makes it possible to construct a responsive system requiring approximately 2–3 min to achieve steady-state ammonia decomposition coupled with the ability to halt the reaction completely in under a minute by cutting off the power supply. Furthermore, by varying the induction heater's power output the magnetic field's amplitude is regulated, which, in turn, determines the catalyst bed's temperature, enabling a tunable H_2/NH_3 ratio ranging from 0–100%.

Results and Discussion

Synthesis and Catalyst Structure

The magnetic nanocomposite CN–A-Ru catalyst was prepared by modifying our previously published procedure.[33,36] The procedure is based on the hydrolysis of AlN in a colloidal suspension of magnetic nanoparticles. Hydrolysis yields AlOOH nanosheets encapsulating the magnetic nanoparticles and thus forming a nanocomposite. The hydrolysis of the AlN powder in the colloidal aqueous suspension of magnetic nanoparticles leads to the decomposition of the AlN particles, saturating the suspension with ammonium and aluminium species.[37] The aluminium species then condensate, which leads to the nucleation and growth of microporous, lamellar or nanosheet-like aggregates of boehmite (γ-AlOOH)[38] encapsulating the magnetic nanoparticles. The possibility of such nanoparticle encapsulation was already extensively studied.[33,36] The γ-AlOOH is dehydrated to alumina at elevated temperatures, resulting in the topotactic transformation of the boehmite to γ-Al_2O_3 while the morphology remains practically unchanged.[33,36] In this case we embedded $Co_{0.67}Ni_{0.33}$ precursor nanoparticles in the AlOOH. The heat treatment was conducted in a H_2 atmosphere to simultaneously dehydrate the AlOOH and reduce the precursor nanoparticles to $Co_{0.67}Ni_{0.33}$ alloy nanoparticles, yielding a CN–A. An alloy of Co and Ni was used for the magnetic nanoparticles as they retain their magnetic properties when exposed to the reducing conditions in the reactor.[35] In the final step, the Ru catalytic nanoparticles were deposited on the surface of the CN–A, yielding CN–A-Ru. The room-temperate magnetization curve of the CN–A-Ru indicates soft ferromagnetic properties characterized by a narrow hysteresis loop (Figure 1a). The XRD powder pattern of the CN–A-Ru is composed of two relatively intense and narrow peaks that are positioned in between the (111) and (200) reflections characteristic for *fcc* Co and Ni,

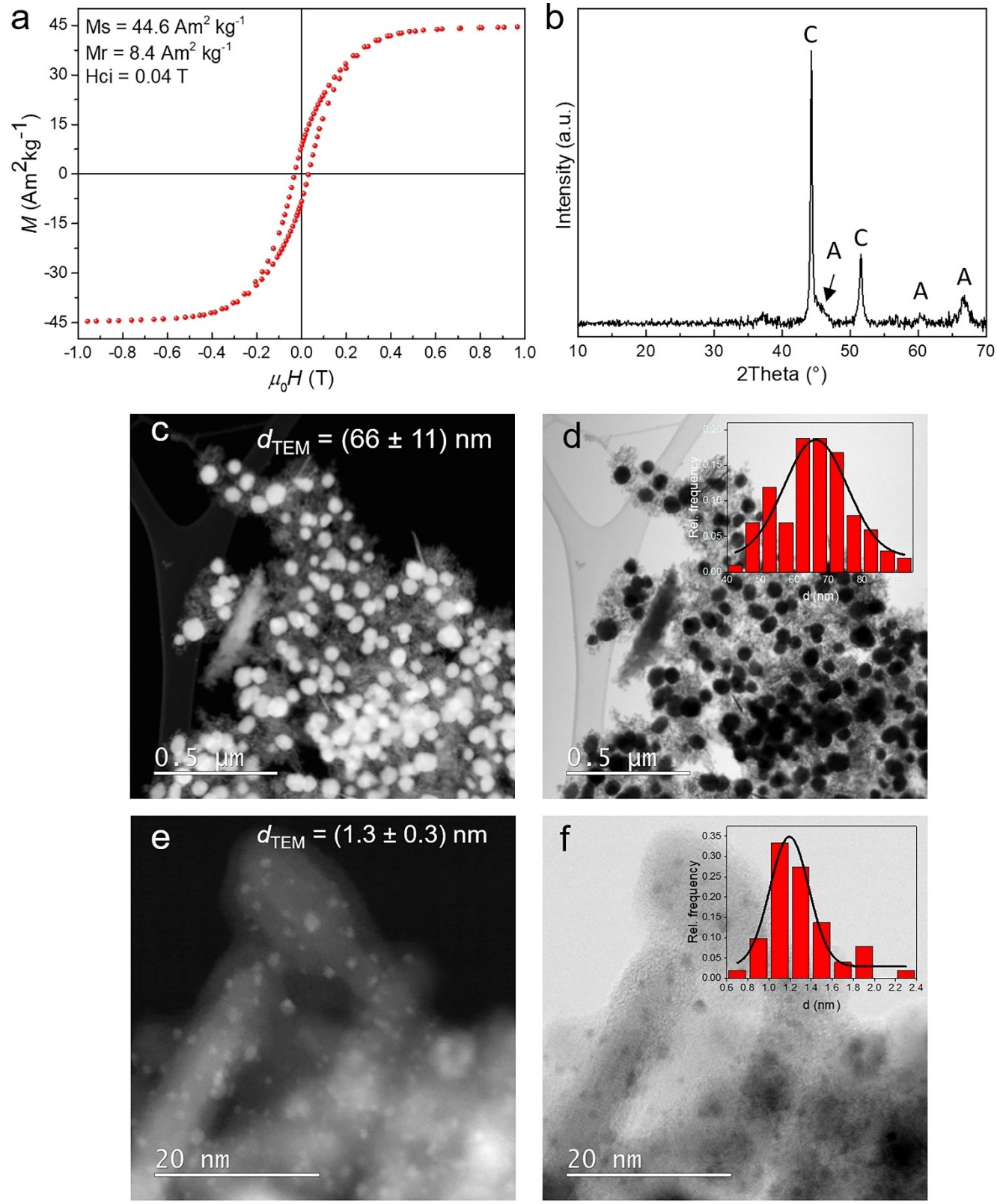

Figure 1. Magnetic properties, X-ray diffraction pattern and electron microscopy of the CN–A-Ru catalyst. A) Room-temperature magnetization curve. B) XRD powder pattern. c), e) HAADF and d), f) BF STEM images. Insets in d), f) are empirical size distributions of $Co_{0.67}Ni_{0.33}$ (d) and Ru (f) nanoparticles fitted with a Gaussian curve. In b reflections of cubic $Co_{0.67}Ni_{0.33}$ are marked with C while alumina is marked with A.

indicating the formation of alloy nanoparticles with a cubic structure. In addition, three broad, low-intensity reflections characteristic for tetragonal Al_2O_3 are visible, indicating the small size of the alumina crystallites (Figure 1b), consistent with alumna prepared by the hydrolysis of AlN.[12]

A scanning–transmission electron (STEM) microscope coupled with an energy-dispersive X-ray spectrometer (EDXS) was used to observe the morphology and composition of the CN–A-Ru (Figure 1c–f). Observations at a lower magnification (Figure 1c and d) revealed a homogenous distribution of $Co_{0.67}Ni_{0.33}$ nanoparticles (seen as bright particles in high-angle annular dark-field (HAADF) or dark particles in bright-field (BF) STEM images within the alumina matrix. Their estimated average size is 66 nm ± 11 nm. A quantitative EDXS analysis of several individual $Co_{0.67}Ni_{0.33}$ nanoparticles showed an even composition with average Co and Ni contents of 69 at% and 31 at%, respectively. Both values are close to the stoichiometric ratio defined by the synthesis route. The BET surface area is moderately high at 137 m^2/g. The STEM observations clearly show a homogenous distribution of approximately 1.3-nm-sized Ru nanoparticles on the surface of the alumina nanosheets in the CN–A-Ru (Figure 1e and f), while the Ru dispersion D_{TEM} = 0.74 was calculated using relationships described by A. Borodziński *et. al.*[39] The Ru nanoparticles predominantly lay on the surface of the alumina nanosheets (Figure 1e and f) because those contribute the majority of the surface area; however, as the alumina coating is macro and mesoporous[33,38] some of the Ru nanoparticles are most likely situated on the surface of the $Co_{67}Ni_{33}$ nanoparticles as well. The measured amount[40] of elemental Ru was determined to be 2.7 wt%, while the Ru surface concentration was found to be 207.3 $\mu mol\,g^{-1}$ (see SI for details regarding CO PA).

Catalytic Ammonia Decomposition over CN-A-Ru

Isothermal Stationary Conditions (IS)

The catalytic performance of the CN–A-Ru nanocomposite was tested for magnetically heated ammonia decomposition. A reactor setup dedicated for magnetically heated ammonia-decomposition testing was designed and built (detailed description in Experimental part and Figure S1). A reactor tube made of quartz was implemented to avoid any magnetic shielding effects. The CN–A-Ru catalyst bed was carefully positioned in the central part of the reactor tube where a constant magnetic field strength is assured. Prior to the catalytic activity testing, the reactor was purged and the catalyst was treated with H_2 at 350 °C for 20 min. Magnetization of the CN–A-Ru catalyst stored at room temperature in air initially drops by approximately 20% due to the partial oxidation and evens out during the course of several weeks, indicating the passivation of the $Co_{0.67}Ni_{0.33}$ nanoparticles. When magnetically heated to 350 °C in a H_2 atmosphere, the power required to maintain 350 °C drops and stabilizes within 10 min, indicating complete reduction of the passivated nanoparticles and restoration of their magnetic properties (reducing at higher temperatures did not further improve their magnetic properties). Since the CN–A-Ru is composed of large amounts of CoNi alloy, which could be active for ammonia decomposition,[41] we initially tested the activity of the Ru-free CN–A material. As predicted, the CN–A shows moderate activity for ammonia decomposition (Figure S2). The conversion increases with temperature and approaches 100% at 500 °C (Figure S2). Increasing the volumetric flow and thus improving the GHSV did not change the conversion at a specified temperature significantly, indicating that it was not kinetics but transport (heat and/or mass) phenomena that were limiting the conversion. The results suggest that further explorations of this noble-metal-free catalyst are needed; however, for the purpose of this study, the important finding is that the activity of the $Co_{0.67}Ni_{0.33}$ is modest in the temperature range between 300 °C (zero conversion) and 400 °C (approx. 20%) (Figure S2). A preliminary test showed that the CN–A-Ru was too active and the reactor was not operated in the kinetic regime, even when subjected to the highest-possible volumetric flow (the conversion remained constant after the flow of 10 vol% NH_3 in Ar was doubled). For this reason, we diluted the CN–A-Ru with CN–A to reach 33 wt% of CN–A-Ru. After the final reduction within the reactor using magnetic heating, the catalyst bed was cooled and the gas flow was switched from 30 vol% H_2 in Ar to 10 vol% ammonia in Ar. After purging, the temperature of the catalyst bed was set to 310 °C, which resulted in a conversion of 32.9% at a gas flow of 30 mL/min. While maintaining the temperature by increasing the power level as needed, the initial 30 mL/min flow rate was doubled. The resulting conversion was 16.6%, which confirmed the operation taking place within the kinetic regime. At this point the temperature of the catalyst bed had been lowered until no conversion was detected and then increased in steady intervals until 100% conversion was achieved. Figure 2a shows the dependence of the ammonia conversion (30 mL/min, 10 vol% in Ar) in relation to the corresponding temperatures measured within the catalyst bed. The conversion increased with the temperature, which is consistent with the endothermic nature of the reaction. Starting at 290 °C, a 13.0% conversion was recorded and nearly all the ammonia was decomposed at 400 °C.

As is evident from Table 1, the activity in terms of TOF value of our catalyst under isothermal, stationary conditions outperforms Ru-based catalysts for a similar size of Ru nanoparticles; however, it is inferior to catalysts composed of larger Ru nanoparticles. The effectiveness of the catalyst can therefore be improved by using Ru nanoparticles of larger size (close to 8 nm). The activity in terms of the rate of ammonia decomposition is very close to the best-performing catalyst (Table 1). The power consumed by the induction heater was determined at an electrical outlet with a power meter. The unit required 535 W to maintain the catalyst bed at 290 °C and 642 W for 400 °C. In this temperature range, the relationship between the two remained linear. The energy efficiency of the process can be further enhanced by improving the magnetic properties of the catalysts, the reactor design and the induction heater.[34,42,43] Namely, the heating properties of the magnetic nanoparticles strongly depend on their composition, their size and homoge-

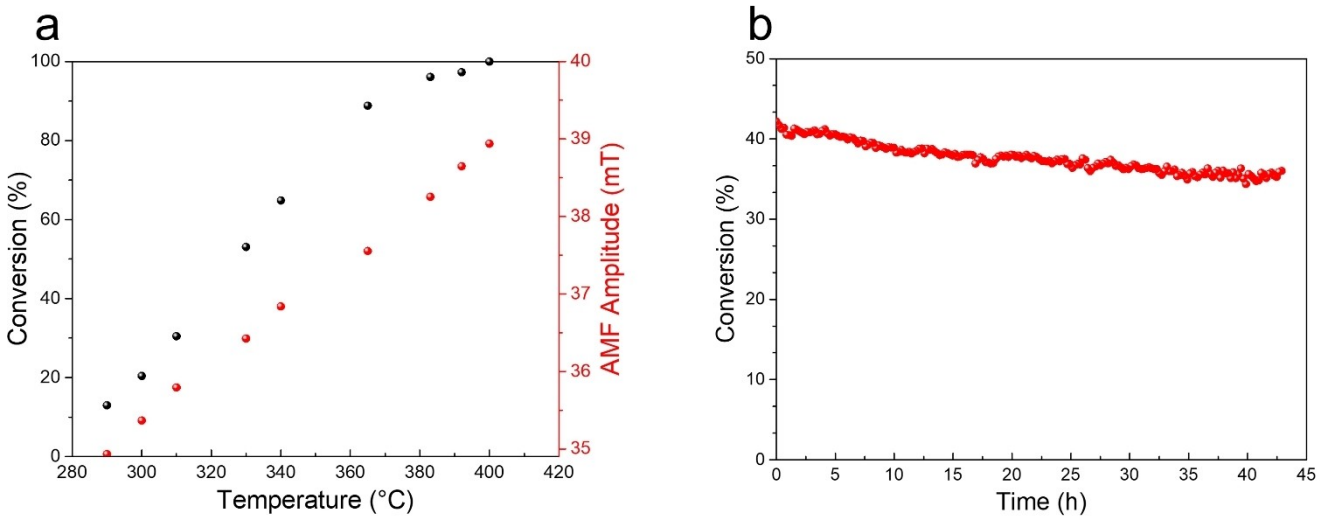

Figure 2. Ammonia decomposition results. a) Ammonia conversion during its decomposition as a function of catalyst bed's temperature (black dots) and AMF amplitude required to reach set temperature (red dots). b) Catalyst stability tests for ammonia decomposition at 320 °C.

Table 1. Comparison of ammonia decomposition over several types of Ru-based catalysts.

Catalyst	Ru loading (%)	Ru Particle size (nm)	Feed gas	Temp. (°C)	TOF_{NH3} (s^{-1})	Rate (μmol_{NH3} g_{Ru}^{-1} s^{-1})	Ref.
Ru/γ-Al_2O_3	1.6	0.8	10 % NH_3 in He, total flow 200 mL min^{-1}	350	0.02	/	[44]
Ru/γ-Al_2O_3	1.6	1.3	10 % NH_3 in He, total flow 200 mL min^{-1}	350	0.05	/	[44]
Ru/γ-Al_2O_3	1.6	7.0	10 % NH_3 in He, total flow 200 mL min^{-1}	350	1.50	850	[44]
Ru/γ-Al_2O_3	4.7	8.8	Molar ratio NH_3/He = 2/1, total flow 60 mL min^{-1}	350	0.30	/	[45]
Ru/γ-Al_2O_3/LiOH	4.7	8.8	Molar ratio NH_3/He = 2/1, total flow 60 mL min^{-1}	350	1.96	/	[45]
Ru/AC	5.0	4.1	Pure NH_3, total flow 50 mL min^{-1}	350	0.11	510	[3]
Ru/CNTs	5.0	3.9	Pure NH_3, total flow 50 mL min^{-1}	350	0.23	510	[3]
Ru/γ-Al_2O_3	5.0	8.7	Pure NH_3, total flow 50 mL min^{-1}	350	0.33	510	[3]
Ru/MgO	5.0	9.1	Pure NH_3, total flow 50 mL min^{-1}	350	0.50	680	[3]
Ru/K-CNT	5.0	3.7	Pure NH_3, total flow 50 mL min^{-1}	350	0.63	1190	[3]
Ru/ZrO_2	5.0	9.4	Pure NH_3, total flow 50 mL min^{-1}	350	0.31	510	[3]
Ru/ $Co_{0.67}Ni_{0.33}$-Al_2O_3	0.67 [a]	1.3	10 % NH_3 in Ar, total flow 30 mL min^{-1}	350	0.15	1111	This work

[a] CN–A-Ru contained 2 wt % of Ru; however, for catalytic testing the CN–A-Ru was diluted with CN–A to reach 0.9 wt % of Ru.

neity of their distribution within the support material. Furthermore, optimizing the geometry of the reactor and the heating coil to achieve the optimal conversion of magnetic energy into heat will improve the energy efficiency as well. The equilibrium conversion is 100 % across the whole studied temperature range, meaning that our system reached equilibrium conversion at approximately 400 °C. The conversion approached equilibrium with a curvature, further indicating that the catalyst is operating at its kinetic limit, i. e., the conversion is limited by the reaction kinetics rather than heat or mass transfer (Figure 2a). Vinum et al. made a similar observation for magnetically heated, steam-methane reforming (SMR), which is in stark contrast to the externally fired case where the heat transfer limits the reactor's performance.[35]

The stability of the CN–A-Ru under magnetically heated ammonia decomposition was assessed over the course of approximately 2 days at a constant temperature of 320 °C and a gas flow of 30 mL/min (Figure 2b). After 43 h on stream, the initial conversion of 42.2 % dropped to 36.0 % over the course of approximately 38 hours of testing. For the last 5 hours, it remained constant. A detailed STEM analysis and CO chemisorption of the spent (after all tests, see below) CN–A-Ru was performed to detect the causes of eventual stabilization. Based on the STEM observations, no visual change to the CN–A-Ru

could be detected. An analysis of the $Co_{0.67}Ni_{0.33}$ nanoparticles showed that their composition as well as their size remained unaltered. For the fresh catalyst, d_{TEM} was determined to be 66 nm ± 11 nm (Figure 1c and d), and for the spent counterpart 66 nm ± 17 nm (Figure 3a and b). More importantly, the Ru nanoparticles retained their size as well. For the fresh catalyst, a d_{TEM} of 1.3 nm ± 0.3 nm (Figure 1e and f) was determined, and for the spent version 1.3 nm ± 0.2 nm (Figure 3c and d). Also, no noticeable Ru particle agglomeration was observed. In addition, the CO chemisorption of the spent CN–A-Ru showed a Ru surface concentration of 67.4 μmol g^{-1}. The value is approximately one-third of 207.3 μmol g^{-1}, the amount found in the fresh catalyst (spent is diluted to 1/3). All the characterizations suggest that we can exclude the growth or agglomeration of the Ru nanoparticles and thus any depletion of the active sites. Additionally, charring can be excluded since no C-containing reagents are present. Therefore, the observed stabilization could be a consequence of compacting the catalyst bed during operation, channeling of the reactive gases or other less-common structural changes that are not detectable by STEM and CO chemisorption. As the deactivation is rather low, we omitted determining its reasons; however, our future work will be devoted to it as industrial applications require well-scrutinized catalysts.

Non-Isothermal Dynamic Experiments (NID)

Non-isothermal dynamic experiments were conducted to assess the temporal dynamics of the ammonia decomposition and consequently the hydrogen production at three different AMF amplitudes. Such tests are important to evaluate the developed process for applications where a rapid system response is important, such as in utilizing intermittent renewable electricity or producing hydrogen on demand, to mention the two most obvious cases. Three different AMF amplitudes were used to achieve rapid heating of the catalyst. The AMF was abruptly turned ON, while the effluent of the reactor was continuously monitored with a mass spectrometer, yielding the composition every second. The bed's temperature was monitored continuously as well. After achieving a steady state, the AMF was turned OFF. Three consecutive pulses were performed (Figure 4).

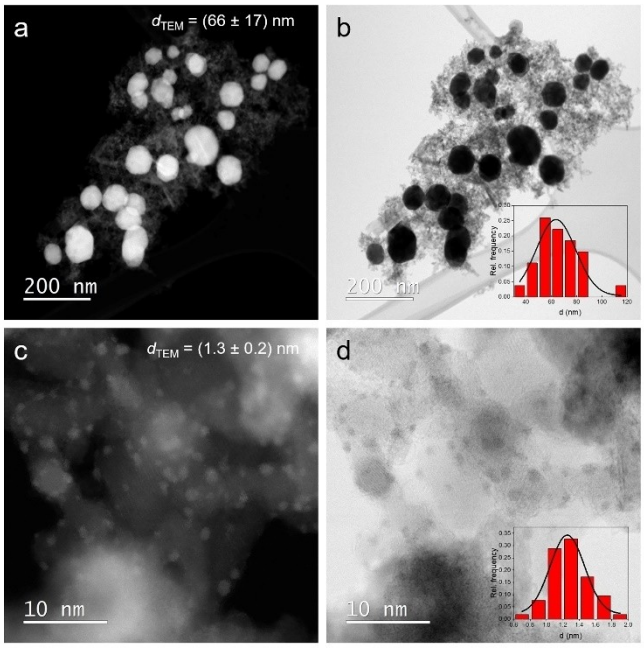

Figure 3. Electron microscopy of the spent CN–A-Ru catalyst. a, c HAADF and b, d BF STEM images.

At 35.4 mT and 38.0 mT, the desorption peaks of the ammonia (ammonia slip) and hydrogen can be clearly seen as narrow peaks extending above the baseline at approximately 150–200 °C. Since ammonia decomposition ensued at just below 300 °C, both peaks can be explained by desorption from the catalyst surface, which adsorbed both gases, while the bed was at a lower temperature. At 48.0 mT the temperature increase was substantially faster and the desorption peaks are no longer resolved. Complete conversion was achieved within approximately 2–3 min. To check for the reproducibility the pulses were plotted for the same time interval (Figure S3). For the sake of clarity only the H_2 signal was plotted (Figure S3). The temperature at the AMF amplitude of 35 mT varied by approximately 4 °C among the pulses, while for the highest field the variation was lowered to approximately 2 °C (Figure S3). The H_2 content in the effluent lagged the variations in the temperature profile with longer dynamics at the lowest AMF field amplitude (Figure S3). To achieve a faster response and better control of the effluent's composition a suitable PID regulation of the induction heater's power could be implemented, yielding an instantaneous ammonia decomposition accompanied by stable H_2 production without any excessive loss of the electrical energy. Recently, K. Nagaoka *et. al.* showed that ammonia decomposition can be initiated from room temperature without an external heat source using a well-designed acidic RuO_2/g-Al_2O_3 catalyst.[46] The catalyst heats up due to ammonia adsorption on alumina, while additional heat needed to decompose the ammonia comes from the oxidative decomposition of ammonia.[46] The autothermal process shows the almost immediate production of H_2 and excels in terms of long-term stability; however, the authors did not show that the process can control the H_2-to-ammonia ratio.

Bringing Theory and Experiment Together

To gain a better insight into the catalyst's performance, extensive DFT and micro-kinetic modelling were employed. The DFT calculations were used to calculate the thermodynamics and kinetics (activation energies and adsorption energies) for the ammonia-decomposition reaction on ruthenium. Ru (0001) was chosen as the most stable (extended) facet of ruthenium, which is also the most exposed in nanoparticles.

The energy profile along the reaction coordinate (relative energies of the intermediate structures and transition states (TSs)) is shown in Figure 5. The rate-determining step for the overall reaction is the recombination of two nitrogen atoms

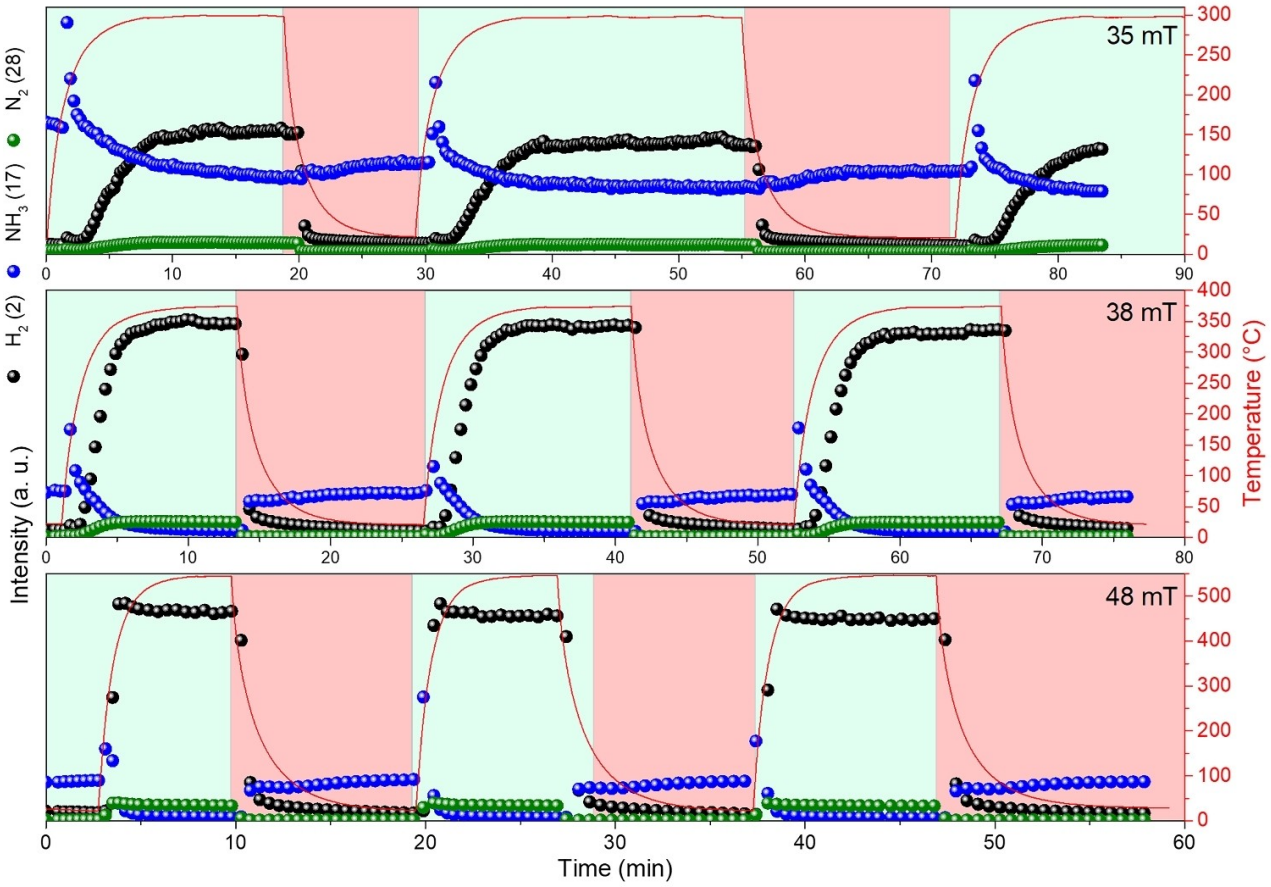

Figure 4. Ammonia decomposition under non-isothermal dynamical conditions. Real-time effluent composition and bed temperature for non-isothermal dynamic experiments performed at AMF amplitudes of 35.4 mT, 38.0 mT and 48.0 mT. The highlighted areas mark the time intervals when the heating was turned on (green) and off (red).

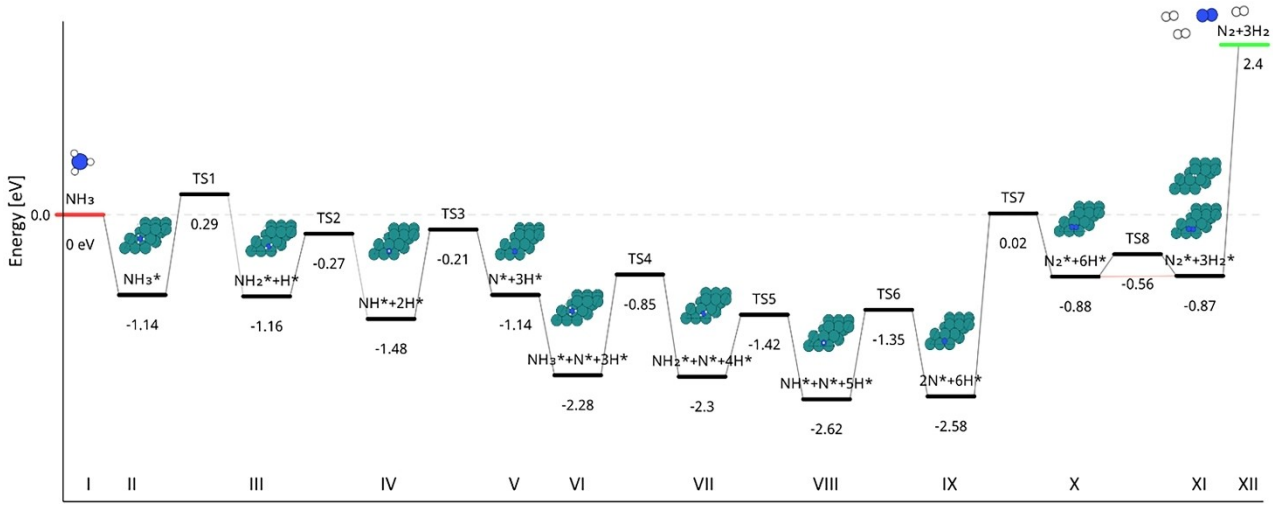

Figure 5. Scheme of the reaction mechanism on Ru (0001) surface.

(TS7, $E_A = 2.60$ eV), while in the decomposition of NH_3 it is the first N–H cleavage that is slowest (TS1, $E_A = 1.43$ eV).

A micro-kinetic model (see SI for details) was constructed to link the parameters of the elementary reaction-step values (from theoretical DFT) with the experimentally determined conversion of NH_3 to H_2 and N_2. The activation energies calculated by DFT listed in Table S1 were used in the micro-kinetic model without further refinement by the regression analysis to avoid overfitting. Instead, we refined the pre-exponential factors of the individual reaction steps with a

regression analysis, which in turn affected the reaction rates. The pre-exponential factors were assumed to be constant regardless of the temperature, which is in general not true but can be assumed when the investigated temperature range is small.

This was completed, as follows. First, all the reaction-rate constants were set to a similar initial value, after which the regression analysis was initiated. The experimentally determined NH_3 conversions of the IS were used to determine the first approximation of all the reaction-rate constants. Figure 6 shows the deviation between the experimentally determined NH_3 conversions and the conversions predicted by the model. The experimentally determined conversions agree well with the conversions predicted by the model, especially at higher temperatures. Additionally, the Weisz-Prater (WP) parameter was calculated[47,48] (calculation method in ESI) to rule out any internal mass-transfer limitations. The WP parameter for the first reaction, i.e., the deprotonation of NH_3 to NH_2, was determined to be 2.6×10^{-4}, a value well below 0.1, clearly indicating that the internal mass limitations are negligible. After the initial determination of the parameters, the same reaction-rate, adsorption and desorption constants were used to predict the concentration profiles of the NH_3, H_2 and N_2 during the NID experiments, where the temperature was rapidly increased and decreased by induction heating. As mentioned in Section *NID*, three different powers were used to heat the catalyst bed to 300 °C, 375 °C and 550 °C. Figure 7 shows the concentration and time profiles determined experimentally and predicted by the model.

After a detailed examination of the experimentally determined concentrations of all three gases, we observed a gradual increase in NH_3 concentration at the reactor outlet after the temperature dropped back to its initial value (approximately 25 °C). More specifically, after the temperature dropped back to its initial value and just before the start of the second rapid heat-up, the NH_3 concentration at the outlet did not settle back to the NH_3 concentration at the inlet, but was lower even though the reaction did not take place. In addition, the NH_3 concentration detected at the effluent was higher than the concentration at the inlet as soon as the rapid heating started. Since the support material of the catalyst contains acidic sites where NH_3 can adsorb and desorb but not react further, we modified the NID model and added another coverage balance

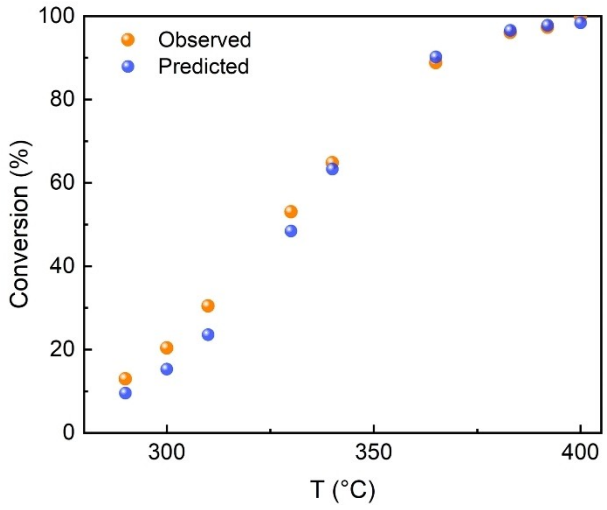

Figure 6. Comparison of predicted and experimental ammonia conversions. Orange dots represent experimentally observed conversion values of ammonia decomposition in isothermal stationary experiments, while blue dots represent the values predicted by the model.

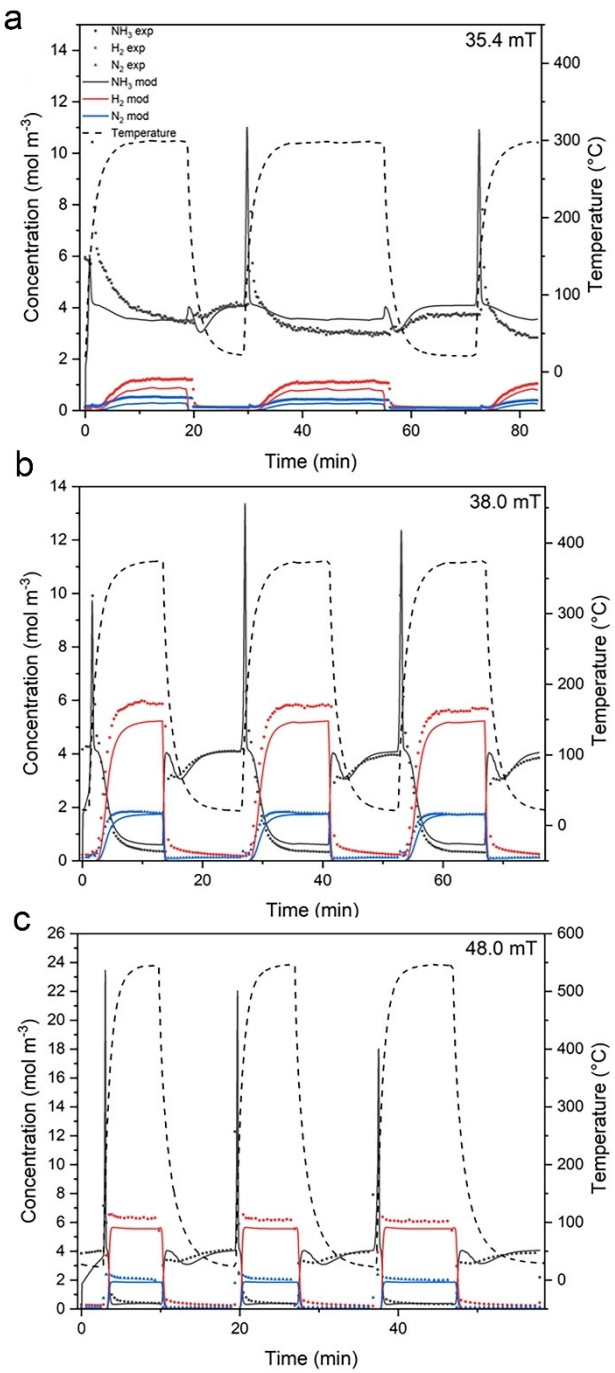

Figure 7. Experimental and model-predicted concentration vs. time profiles of NH_3, H_2 and N_2 in a non-isothermal dynamic experiment. AMF amplitudes of $B_{max} = 35.4$ mT, b $B_{max} = 38.0$ mT and c $B_{max} = 48.0$ mT were used to heat the catalyst's bed.

for the adsorption and desorption of NH_3. In this way, the deviation of the NH_3 concentration in this time interval could be solved. The rapid increase in NH_3 concentration after heating could also be described well.

A comparison of the IS and NID models shows that the NH_3 conversion proceeds only slowly at a temperature in the catalyst bed of 300 °C or below. Between 300 and 375 °C, the conversion of NH_3 is much faster, and at temperatures exceeding 400 °C (Figure 7c) the conversion to H_2 and N_2 is instantaneous. Compiled parameters from both experiments are presented in Tables S2–S4.

Pure Ammonia Decomposition over CN-A-Ru

Studying the decomposition of diluted ammonia (modeling of experimental results) gave us a valuable insight into the reaction mechanism, the relevant kinetic parameters and the dynamics of the process; however, for technological applications the decomposition of pure ammonia is more interesting. We used the same catalyst and the reactor setup as used for the studies of diluted ammonia. The only difference was that we used an inhouse-written python PID control loop enabling better control of the catalyst's bed temperature. Figure 8a shows the temperature dependence of the ammonia conversion (18 mL/min, pure ammonia, 154 mg of the CN–A-Ru; 0.9 wt% of Ru in total). Also, in this case the conversion increased with the temperature, starting at 310 °C with a 5.0% conversion and reaching 99.1% conversion at 525 °C, while 100% was reached at 525 °C. The calculated rate at 350 °C was 2011 $\mu mol_{NH3}\, g_{Ru}^{-1}\, s^{-1}$, which is nearly twice as much as in the case of diluted ammonia (Table 1), indicating good activity of the catalyst in pure ammonia. The increase in rate is expected as the amount of ammonia in the inlet stream increased by 10× in comparison to the diluted ammonia (10 vol% in Ar). Because the rate increased only twice, the temperature dependence of the conversion in the case of pure ammonia is shifted to higher temperatures, although the amount of converted ammonia is larger. In order to further increase the amount of converted ammonia and consequently shift the conversion curve towards lower temperatures, the quantity of Ru catalytic nanoparticles would have to be increased. The long-term stability was tested at 425 °C for 90 hours (Figure 8b). Within approximately 5 hours, the initial conversion dropped from 61% to 59%, and for the remaining time varied between 59 and 57%. Similar behaviour was found when diluted ammonia was used; however, in the latter case the stabilization period was longer and the conversion drop was more pronounced. In both cases the temperature of the bed was stable and the field needed to maintain the temperature over the course of testing was constant, indicating stable magnetic performance. In addition to the characterizations of the spent catalyst described in the Section *Isothermal stationary conditions (IS)* we measured a magnetization curve of the spent catalyst at room temperature (Figure S4). A comparison to the magnetization curve of the fresh catalyst shows practically no change in the magnetic properties (Figure S4). With no detectable change in the size of the Ru nanoparticles, the surface atoms' concentration and constant magnetic properties we can reasonably assume that the stabilization is caused by less obvious structural changes to the bed, such as packing, for example, and that the catalyst does not undergo deactivation.

Conclusions

In our experimental work we demonstrated a previously unexplored method of magnetically heated ammonia decomposition to produce on-demand hydrogen. The ferromagnetic $Co_{0.67}Ni_{0.33}$ alloy nanoparticles incorporated within the large-surface-area alumina catalyst support serve as an effective medium to convert the AMF energy to heat, while the deposited Ru

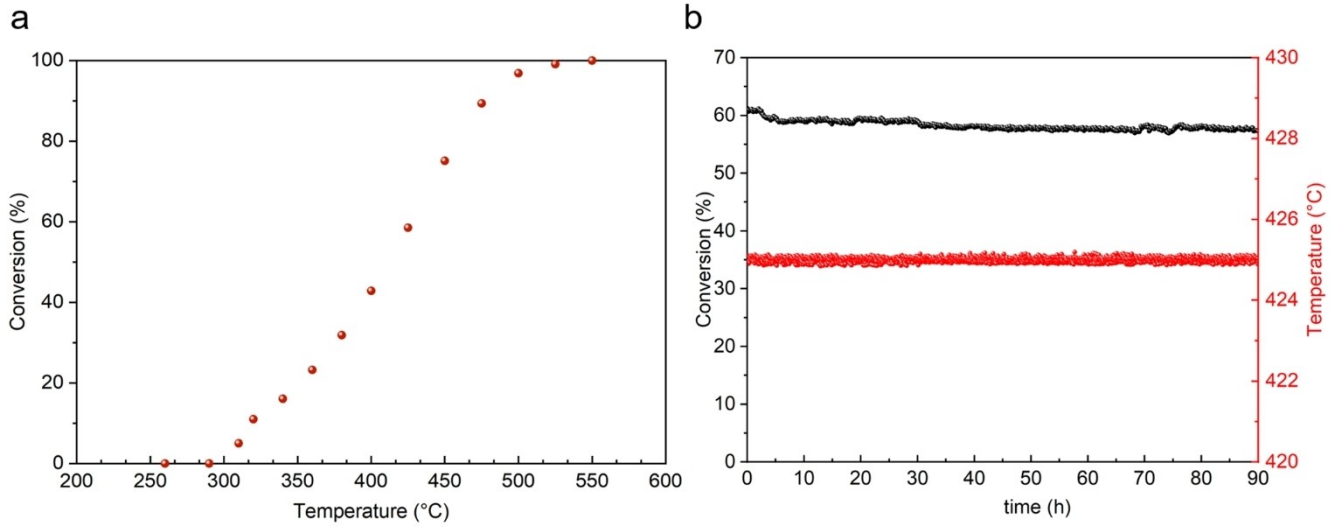

Figure 8. Pure ammonia conversion during its decomposition as a function of catalyst bed temperature a) and catalyst stability tests for ammonia decomposition at 425 °C (black dots conversion, red dots temperature) b).

nanoparticles serve as an active catalyst. The key feature is rapid heating of the magnetic nanoparticles, which enables rapid changes to the catalyst's temperature and consequently the effluent's composition. The H_2-to-NH_3 ratio in the effluent can be tuned from 0–1 on the time scale of a minute. Examining the NH_3 conversion under isothermal, stationary conditions revealed that the kinetics hampered the conversion and not the heat transfer, as is usually the case in conventionally heated reactors. The implementation of magnetic heating in ammonia decomposition has the potential to address the on-demand release of hydrogen from a stable carrier, producing tunable H_2-to-NH_3 ratios needed for internal combustion engines and the utilization of intermittent renewable electricity in a single unit.

Acknowledgements

This research was supported by the Slovenian Research Agency (Research Core Funding P2-0089 and Young Researcher Scheme Contract 1000-18-0106). B. L. appreciates the funding from the Slovenian Research Agency (core funding P2-0152). M. H. was funded by the project N1-0303 and infrastructure funding I0-0039. M. G. was funded by the project N2-0242. Financial support for longer-term large collaborative research and innovation programme at TRL 3–6 level HyBReED under the Roadmap for Recovery and Resilience is also acknowledged.

Conflict of Interests

S.G., Ž.P., B.L, A.S., D.M. and J.T. are listed as co-inventors of a "Fast Dynamically Responsive Ammonia Synthesis or Cracking for H2 Storage Utilising Structured Magnetically-heated Catalysts" patent application (LU506256). The patent describes a method for quickly tunable on-demand gas phase reactions of ammonia decomposition to produce hydrogen and nitrogen gas and reversible reaction of ammonia synthesis from hydrogen and nitrogen gas by use of magnetic heating, the corresponding catalyst materials, their preparation procedures and a reactor system designed specifically for gas-phase magnetic catalysis. The remaining authors declare no competing interests.

Data Availability Statement

The data that support the findings of this study are available from the corresponding author upon reasonable request.

Keywords: Heterogenous catalysis · Magnetic properties · Magnetic catalysis · Ammonia decomposition · Ruthenium

[1] I. Lucentini, X. Garcia, X. Vendrell, J. Llorca, *Ind. Eng. Chem. Res.* **2021**, *60*, 18560–18611.
[2] F. R. García-García, Y. H. Ma, I. Rodríguez-Ramos, A. Guerrero-Ruiz, *Catal. Commun.* **2008**, *9*, 482–486.
[3] S.-F. Yin, Q.-H. Zhang, B.-Q. Xu, W.-X. Zhu, C.-F. Ng, C.-T. Au, *J. Catal.* **2004**, *224*, 384–396.
[4] Y.-Q. Zou, N. von Wolff, A. Anaby, Y. Xie, D. Milstein, *Nat. Catal.* **2019**, *2*, 415–422.
[5] R. Sang, Z. Wei, Y. Hu, E. Alberico, D. Wei, X. Tian, P. Ryabchuk, A. Spannenberg, R. Razzaq, R. Jackstell, J. Massa, P. Sponholz, H. Jiao, H. Junge, M. Beller, *Nat. Catal.* **2023**, *6*, 543–550.
[6] S. Chen, J. Jelic, D. Rein, S. Najafishirtari, F.-P. Schmidt, F. Girgsdies, L. Kang, A. Wandzilak, A. Rabe, D. E. Doronkin, J. Wang, K. Friedel Ortega, S. DeBeer, J.-D. Grunwaldt, R. Schlögl, T. Lunkenbein, F. Studt, M. Behrens, *Nat. Commun.* **2024**, *15*, 871.
[7] H. Fang, S. Wu, T. Ayvali, J. Zheng, J. Fellowes, P.-L. Ho, K. C. Leung, A. Large, G. Held, R. Kato, K. Suenaga, Y. I. A. Reyes, H. V. Thang, H.-Y. T. Chen, S. C. E. Tsang, *Nat. Commun.* **2023**, *14*, 647.
[8] I. Lucentini, G. García Colli, C. D. Luzi, I. Serrano, O. M. Martínez, J. Llorca, *Appl. Catal., B* **2021**, *286*, 119896.
[9] X. Han, M. Hu, J. Yu, X. Xu, P. Jing, B. Liu, R. Gao, J. Zhang, *Appl. Catal., B* **2023**, *328*, 122534.
[10] X.-Y. Guo, J.-H. Wang, Q. Zhang, T.-Z. Li, H. Dong, C.-J. Jia, C. Li, Y.-W. Zhang, *Appl. Catal., B* **2024**, 123844.
[11] E. Nadimi, G. Przybyła, M. T. Lewandowski, W. Adamczyk, *J. Energy Inst.* **2023**, *107*, 101158.
[12] K. Kuta, G. Przybyła, D. Kurzydym, Z. Żmudka, *Fuel* **2023**, *334*, 126523.
[13] A. Valera-Medina, H. Xiao, M. Owen-Jones, W. I. F. David, P. J. Bowen, *Prog. Energy Combust. Sci.* **2018**, *69*, 63–102.
[14] C. S. Mørch, A. Bjerre, M. P. Gøttrup, S. C. Sorenson, J. Schramm, *Fuel* **2011**, *90*, 854–864.
[15] W. Wang, J. M. Herreros, A. Tsolakis, A. P. E. York, *Int. J. Hydrog.* **2013**, *38*, 9907–9917.
[16] M. Comotti, S. Frigo, *Int. J. Hydrog.* **2015**, *40*, 10673–10686.
[17] J. Hwang, R. R. Rao, L. Giordano, K. Akkiraju, X. R. Wang, E. J. Crumlin, H. Bluhm, Y. Shao-Horn, *Nat. Catal.* **2021**, *4*, 663–673.
[18] Y. Li, G. Li, Y. Zou, W. Liu, H. Zhang, S. Lu, Z. Li, S. Zhang, H. Peng, *Appl. Catal., B* **2024**, *344*, 123612.
[19] T. E. Bell, L. Torrente-Murciano, *Top. Catal.* **2016**, *59*, 1438–1457.
[20] K. E. Lamb, M. D. Dolan, D. F. Kennedy, *Int. J. Hydrog.* **2019**, *44*, 3580–3593.
[21] F. Schüth, R. Palkovits, R. Schlögl, D. S. Su, *Energy Environ. Sci.* **2012**, *5*, 6278–6289.
[22] C. J. H. Jacobsen, S. Dahl, B. S. Clausen, S. Bahn, A. Logadottir, J. K. Nørskov, *J. Am. Chem. Soc.* **2001**, *123*, 8404–8405.
[23] A. Badakhsh, Y. Kwak, Y.-J. Lee, H. Jeong, Y. Kim, H. Sohn, S. W. Nam, C. W. Yoon, C. W. Park, Y. S. Jo, *Chem. Eng. J.* **2021**, *426*, 130802.
[24] W. Wang, G. Tuci, C. Duong-Viet, Y. Liu, A. Rossin, L. Luconi, J.-M. Nhut, L. Nguyen-Dinh, C. Pham-Huu, G. Giambastiani, *ACS Catal.* **2019**, *9*, 7921–7935.
[25] R. Hergt, R. Hiergeist, I. Hilger, W. A. Kaiser, Y. Lapatnikov, S. Margel, U. Richter, *J. Magn. Magn. Mater.* **2004**, *270*, 345–357.
[26] S. Ceylan, C. Friese, C. Lammel, K. Mazac, A. Kirschning, *Angew. Chem. Int. Ed.* **2008**, *47*, 8950–8953.
[27] R. H. Soon, Z. Yin, M. A. Dogan, N. O. Dogan, M. E. Tiryaki, A. C. Karacakol, A. Aydin, P. Esmaeili-Dokht, M. Sitti, *Nat. Commun.* **2023**, *14*, 3320.
[28] Q. Zhang, X. Yang, J. Guan, *ACS Appl. Nano Mater.* **2019**, *2*, 4681–4697.
[29] S. R. Yassine, Z. Fatfat, G. H. Darwish, P. Karam, *Catal. Sci. Technol.* **2020**, *10*, 3890–3896.
[30] T. Tatarchuk, N. Danyliuk, I. Lapchuk, A. Shyichuk, V. Kotsyubynsky, *Mater. Today: Proc.* **2022**, *62*, 5805–5811.
[31] Z. Ma, J. Mohapatra, K. Wei, J. P. Liu, S. Sun, *Chem. Rev.* **2023**, *123*, 3904–3943.
[32] S. Gyergyek, D. Lisjak, M. Beković, M. Grilc, B. Likozar, M. Nečemer, D. Makovec, *Nanomaterials (Basel)* **2020**, *10*, 1142.
[33] S. Gyergyek, A. Kocjan, M. Grilc, B. Likozar, B. Hočevar, D. Makovec, *Green Chem.* **2020**, *22*, 5978–5983.
[34] M. R. Almind, M. G. Vinum, S. T. Wismann, M. F. Hansen, S. B. Vendelbo, J. S. Engbæk, P. M. Mortensen, I. Chorkendorff, C. Frandsen, *ACS Appl. Nano Mater.* **2021**, DOI: 10.1021/acsanm.1c01941.
[35] M. G. Vinum, M. R. Almind, J. S. Engbæk, S. B. Vendelbo, M. F. Hansen, C. Frandsen, J. Bendix, P. M. Mortensen, *Angew. Chem. Int. Ed.* **2018**, *57*, 10569–10573.
[36] A. Sedminek, D. Makovec, J. Teržan, B. Likozar, P. Jenuš, A. Kocjan, G. Marolt, S. Gyergyek, *J. Alloys Compd.* **2024**, *1005*, 176109.
[37] A. Kocjan, *Chem. Rec.* **2018**, *18*, 1232–1246.
[38] A. Kocjan, T. Konegger, A. Dakskobler, *J. Mater. Sci.* **2017**, *52*, 11168–11178.

[39] A. Borodziński, M. Bonarowska, *Langmuir* **1997**, *13*, 5613–5620.
[40] M. Nečemer, P. Kump, J. Ščančar, R. Jaćimović, J. Simčič, P. Pelicon, M. Budnar, Z. Jeran, P. Pongrac, M. Regvar, K. Vogel-Mikuš, *Spectrochim. Acta Part B: At. Spectrosc.* **2008**, *63*, 1240–1247.
[41] Z.-W. Wu, X. Li, Y.-H. Qin, L. Deng, C.-W. Wang, X. Jiang, *Int. J. Hydrog.* **2020**, *45*, 15263–15269.
[42] S. Faure, S. S. Kale, N. Mille, S. Cayez, T. Ourlin, K. Soulantica, J. Carrey, B. Chaudret, *J. Appl. Phys.* **2021**, *129*, 044901.
[43] M. R. Almind, S. B. Vendelbo, M. F. Hansen, M. G. Vinum, C. Frandsen, P. M. Mortensen, J. S. Engbæk, *Catal. Today* **2020**, *342*, 13–20.
[44] A. M. Karim, V. Prasad, G. Mpourmpakis, W. W. Lonergan, A. I. Frenkel, J. G. Chen, D. G. Vlachos, *J. Am. Chem. Soc.* **2009**, *131*, 12230–12239.
[45] S. Bajus, F. Agel, M. Kusche, N. Ní Bhriain, P. Wasserscheid, *Appl. Catal., A* **2016**, *510*, 189–195.
[46] K. Nagaoka, T. Eboshi, Y. Takeishi, R. Tasaki, K. Honda, K. Imamura, K. Sato, *Sci. Adv.* **2017**, *3*, e1602747.
[47] M. J. Tang, R. A. Cox, M. Kalberer, *Atmos. Chem. Phys.* **2014**, *14*, 9233–9247.
[48] V.-L. Yfanti, D. Ipsakis, A. A. Lemonidou, *React. Chem. Eng.* **2018**, *3*, 559–571.

Manuscript received: September 9, 2024
Revised manuscript received: December 2, 2024
Accepted manuscript online: December 3, 2024
Version of record online: ■■, ■■